# Unprecedented solar water splitting of dendritic nanostructured $Bi_2O_3$ films by combined oxygen vacancy formation and Mo doping

Maged N Shaddad,[a] Prabhakarn Arunachalam,[a,*] Mohmoud Hezam,[b] Norah M. AL-Saeedan,[a] Sixto Gimenez,[c] Juan Bisquert,[c] Abdullah M Al-Mayouf,*[a,d]

[a] Electrochemical Sciences Research Chair (ESRC), Chemistry Department, College of Science, King Saud University, Riyadh 11451, Saudi Arabia

[b] King Abdullah Institute for Nanotechnology, King Saud University, Riyadh 11451, Saudi Arabia

[c] Institute of Advanced Materials (INAM), Universitat Jaume I, 12006 Castelló, Spain.

[d] K.A.CARE Energy Research and Innovation Center at Riyadh, Saudi Arabia

*Corresponding authors. E-mail addresses: parunachalam@ksu.edu.sa (P. Arunachalam); amayouf@ksu.edu.sa (A. M. Al-Mayouf)

**ABSTRACT**

We demonstrate the synergetic effect of Mo-doping and vacuum-annealing on dendritic nanostructured bismuth oxide ($Bi_2O_3$) thin films prepared by electrodeposition for visible-light-assisted photoelectrochemical (PEC) water oxidation. After evaluating various extents of Mo-doping as well as vacuum-annealing temperatures, it was evidenced that both Mo-doping and vacuum-annealing significantly improved the efficiency and PEC water oxidation performance. Compared to the undoped $Bi_2O_3$ photoanode, the optimized Mo-doped $Bi_2O_3$, after vacuum-annealing, resulted in more than 25-fold enhancement in the photoanodic current density to 1.06 $mA/cm^2$ at 1.23 VRHE under AM1.5 G illumination. The PEC enhancement is credited mainly to the increased PEC surface active sites in the Mo-doped vacuum annealed sample. Confirmed by combined XPS and Mott-Schottky (M-S) analysis, vacuum annealing resulted in surface oxygen vacancies that can contribute to the photocatalytic activity. Besides, Mo-doping resulted in reduced dimensions of the dendritic structure, revealed by FE-SEM and XRD measurements, resulting in larger surface area and, therefore, larger surface/electrolyte contact. This dual strategy (metal doping + vacuum annealing) can be generalized to assemble photoanodes of other materials used for the production of solar fuels.

**Keywords:** β-Bi2O3 nonporous • oxygen vacancies (OVs) • water splitting• surface engineering. Mo doping

## 1. Introduction

To proficiently hinder the depletion of fossil fuels and assuage the associated environmental problems caused by the amassing carbon-dioxide emissions, numerous researchers have attempted to construct new energy-supply systems that are clean and sustainable. Solar-assisted catalysis on semiconductor-based production of clean solar fuels is, generally, a proficient way to assuage environmental concerns and to satisfy the increasing global demands for energy. Photoelectrochemical (PEC) water splitting, with the aid of novel and proficient semiconductor-based materials, has emerged as a promising application in the domain of materials science.[1] During the past years, numerous research works have been performed on different semiconductor-based electrodes for solar-driven water oxidation,[2-5,] but using them as effective photoanodes is still a challenge. The following are the requirements of a proficient electrode for PEC water splitting: the electrode must possess a suitable bandgap (1.6–2.2 eV) with a high absorption coefficient, suitable valence-band (VB) and conduction band (CB) energy positions respectively for oxygen evolution reaction (OER) and hydrogen evolution reaction (HER), high carrier mobility, good photo and chemical stability, and cost-effectiveness.[6–8]

The most widely recognized semiconductor-based electrodes for performing solar-driven water splitting comprise $TiO_2$, ZnO, $BiVO_4$, CuO, and $Fe_2O_3$.[1-2] Particularly, the most common metal oxides, e.g. ZnO and $TiO_2$, have wide bandgaps of approximately 3 eV, as a result of which these oxides absorb only the ultraviolet (UV) region of the solar spectrum (comprising about 4% of solar energy only). Bismuth oxide ($Bi_2O_3$) exhibits exceptional polymorphism having many reported polymorphs (α-, β-, γ-, δ-, ω- and η-$Bi_2O_3$), with other non-stoichiometric polymorphs also exist.[9-13] While the monoclinic α-$Bi_2O_3$ is the stable phase at room temperature for bulk $Bi_2O_3$, tetragonal β-$Bi_2O_3$ is the most stable one for $Bi_2O_3$ nanostructures.[9,14] The stability of the tetragonal phase can, however, be demolished by extrinsic doping.[18] Compared to common UV-absorbing oxides such as ZnO and $TiO_2$, α and β phases have lower bandgaps allowing the absorption in a wider UV-visible range of the solar spectrum.[16-20,24-25] β-$Bi_2O_3$ has a relatively lower bandgap compared to the α-$Bi_2O_3$.[15-16] Additionally, β-$Bi_2O_3$ supports more significant electron transport because of its *c*-axis-oriented tetragonal structure.[17–18] The lone-pair Bi 6s orbital that contributes to the VB reduces the bandgap value and increases the mobility of photogenerated electrons as well.[19] This combined effect, besides the less toxicity, earth abundance, and low cost, makes β-$Bi_2O_3$ an efficient catalyst material for light-induced catalyst in general[17-28] and for solar water splitting in particular.[20-21]

Compared to the other polymorphs, pure β-$Bi_2O_3$ is usually challenging to synthesize at the nanoscale.[17-19] In the literature, β-$Bi_2O_3$ nanostructures or nanostructured films could be suitably fabricated through numerous methodologies, including electrochemical deposition, hydrothermal process, and solid-state reactions.[17, 24–26,30]

The direct use of pure β-$Bi_2O_3$ for solar water splitting has been reported by Hajra et al.[31] to suffer from considerable loss of photocurrent with reduced stability. Further, there have been numerous reports about $Bi_2O_3$ based composites for their photoelectrocatalytic applications.[32-34] Enormous efforts have been made toward introducing metal dopants, such as Mo and W ions in their hexavalent state. Especially, Mo has been of particular interest and has been reported to be a more efficient electron donor because of its generated higher density of states.[39] Up to the extent of our knowledge, published work on Mo-doped $Bi_2O_3$ is almost naught.[40-41] However, these metal dopants are reported to ultimately promote the intrinsic charge transport of $BiVO_4$ oxides by strengthening the lattice distortion.[35-39]

In addition to the extrinsic doping via metal dopants, the creation of surface oxygen vacancies (OVs) has been recognized as an essential strategy to improve the photoelectrochemical performance.[42–43] In addition to increasing the donor density in bulk and thus improving the electron mobility, vacancies formed at the surface can function as active sites for adsorption and PEC reactions.[42,44-46] It has been reported that the surface OVs supply coordinately unsaturated sites to initiate the PEC water oxidation. For instance, various research efforts on surface-OV-induced effects in $TiO_2$,[47] $Bi_2WO_6$,[48] and $Bi_2O_2CO_3$[49] revealed that OVs can considerably promote their photocatalytic activities. We recently reported that the combined effect of both OVs and metal doping could be an efficient strategy to increase the efficiency of solar water splitting. Notably, the combined effect of Zr-doping and stimulation of OVs in $TiO_2$ nanotubes have shown to enhance the visible-light absorption depth and enhanced the separation of the light-induced hole–electron pairs.[50]

Interestingly, a dual strategy to simultaneously modify the $Bi_2O_3$ bulk (by Mo doping) and its surface activity (by simple vacuum annealing) has been successfully applied to obtain, up to the extent of our knowledge, unprecedented water-splitting efficiency of pure $Bi_2O_3$ electrodes. Our strategy reduced the effective bandgap of the prepared electrodes from 3.2 eV down to 2.6 eV in addition to enhanced surface area and improved surface activity. By coupling Mo-doping and surface OVs in nanostructured $Bi_2O_3$ thin films, we achieved an efficient photoelectrode with a photocurrent density of 1.06 $mA.cm^2$ at 1.23 $V_{RHE}$, which is about 25-fold enhancement compared to that of reference $Bi_2O_3$ thin films.

## 2. Experimental Section

*Materials*

Bismuth (III) nitrate ($Bi(NO_3)_3 \cdot 5H_2O$, ≥98.0%) and ethylene glycol (EG, $HOCH_2CH_2OH$, ≥99.8%) were acquired from Fisher Scientific.

*Preparation of β-$Bi_2O_3$ and Mo:$Bi_2O_3$*

The electrochemical deposition was performed in a single cell by using an electrochemical system (Autolab, PGSTAT30). In a typical process, a classical 3-electrode system comprised an FTO substrate as the working electrode, an Ag/AgCl (4 M KCl) reference electrode, and a Pt counter electrode. Subsequently, for preparing Bi-metallic films from EG, an EG solution containing 20 mM $Bi(NO_3)_3 \cdot 5H_2O$ was used. After that, the electrodeposition process of the solution was performed by passing 0.1 C/cm$^2$ at E = −1.8 V vs. Ag/AgCl, followed by subjecting it to a resting time of 2 s. The electrochemical cycle was repeated five times to reach the total charge of 0.50 C/cm$^2$. Subsequently, the obtained Bi films were annealed at 450 °C for 2 h in the air (ramp rate = 3.0 °C/min) to create nanostructured $Bi_2O_3$ thin films. The attained electrodes were cleaned using water and then allowed to air dry. Furthermore, this successive electrochemical deposition was performed to derive the required photoelectrodes. To fabricate Mo: $Bi_2O_3$ photoanodes, 70 µL of sodium molybdate ($Na_2MoO_4.2H_2O$) in the DMSO solution was moved onto the electrodeposited Bi electrode, and, subsequently, the photoelectrode was annealed at 450 °C for 2 h in air. Second, the $Bi_2O_3$ or Mo:$Bi_2O_3$ films were placed into a porcelain combustion boat at 350 °C for various times (0.5 to 5.0 h) under vacuum to obtain oxygen vacancy OV-$Bi_2O_3$/OV-Mo:$Bi_2O_3$. Finally, the electrodes were cooled down naturally, and the pressure was gently released.

*Characterization of $Bi_2O_3$-based films*

The crystalline purity and phases of the materials were recorded via X-ray diffraction (XRD, Rigaku-Mini Flex 600, Japan) under Cu $K_\alpha$ radiation. Absorbance spectra of the fabricated electrodes were analyzed using UV-vis spectroscopy (Shimadzu UV-2600, Japan). Also, the morphological features of the $Bi_2O_3$ thin films were analyzed using field emission SEM (JEOL JSM-7000F, Japan). PEC performance of the fabricated electrodes was studied by evaluating their photocurrent density during water splitting. All the PEC analyses were conducted in 0.1 M phosphate buffer solution (PBS, pH = 7). The photocurrent density was assessed by using a potentiostat (Autolab, PGSTAT30) at the sweep rate of 10 mV/s. Furthermore, electrochemical impedance spectroscopy (EIS) analysis was performed via an electrochemical workstation.

The applied bias photon to current efficiency (ABPE) is given by:

$$ABPE\ (\%) = \frac{J_{PEC}(mA/cm^2) * (1.23 - V_{bias})V}{Pin(mW/cm^2)} \times 100$$

where $J_{PEC}$ denotes the photocurrent density, $V_{bias}$ the applied bias, and $P_{in}$ the incident illumination power density (AM 1.5G).

## 3. Results and Discussion

*Synthesis of Mo:$Bi_2O_3$ thin films*

**Synthesis.** A novel, non-aqueous, electrochemical-deposition method was employed, which was based on the metal-organic precursors of Bi dispersed in EG solution. Then, Mo was introduced to the Bi-metal surface to prepare the thin films of Mo-doped $Bi_2O_3$ with tunable quantities of Mo. Subsequently, the fabricated thin films were subjected to the vacuum-annealing process. The various stages for the fabrication of electrodes are schematically depicted in **Figure 1.**

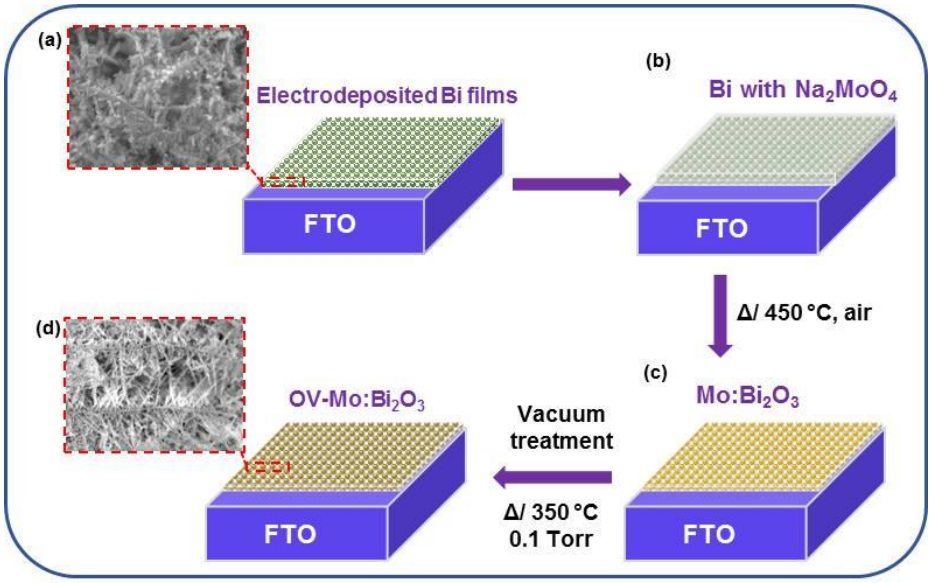


**Figure 1.** Conversion of nanostructured dendritic Bi-metal electrodes to OV-Mo:$Bi_2O_3$ photoelectrodes

*Structural Characterization of Mo-doped $Bi_2O_3$ photoanodes*

To analyze the purity and crystalline nature of the $Bi_2O_3$, OV-$Bi_2O_3$, Mo:$Bi_2O_3$, and OV-Mo:$Bi_2O_3$ thin films, XRD was performed. The XRD spectra for all four electrodes are shown in **Figure 2**. The pure air-annealed $Bi_2O_3$ electrode could be purely indexed with the tetragonal $Bi_2O_{2.3}$ phase (JCPDS No. 01-76-2477). Furthermore, no other peaks corresponding to other phases were noticed, suggesting that $Bi_2O_{2.3}$ was the main phase in the product. This oxygen-deficient polymorph of β-$Bi_2O_3$ was similarly reported to form under thermal oxidation of Bismuth.[20-21] Vacuum annealing of the pure electrodes did not result in any other impurity phase and could be fully indexed to the same $Bi_2O_{2.3}$ phase as well. There was, however, a slight shift on the 2θ axis to the left, see **Figure 2b**, indicating a slight lattice expansion that may be induced by oxygen vacancies. This might imply the creation of neutral oxygen vacancies, which were reported to cause such expansions or a mixture of both neutral and charged oxygen vacancies.[51,52] The only slight shift along

the 2θ axis supports the latter possibility. In addition to the slight shift in peak position, their peak intensities were reduced in the vacuum annealed sample. This effect of vacuum annealing was also present for the Mo-doped sample as well. This can be attributed to the creation of oxygen vacancies by vacuum annealing resulting in reduced crystalline order. As will be discussed below, this slight negative effect was, however, essential to gain the highly efficient photocatalytic activity caused by OVs.

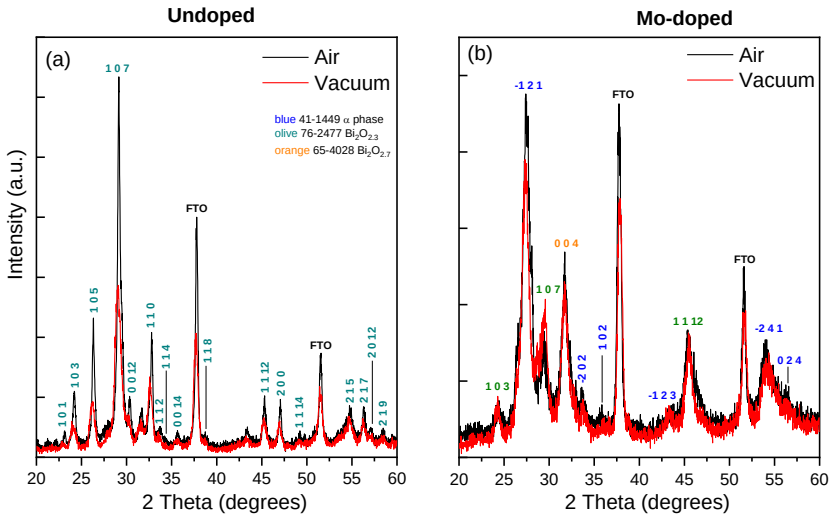


**Figure 2.** Normalized XRD patterns of electrochemically deposited (a) undoped $Bi_2O_3$, (b) Mo-doped OV-$Bi_2O_3$ photoelectrodes, (b).

When $Bi_2O_3$ was doped with Mo, the nanostructured doped film crystallized in a mixture of the original $Bi_2O_{2.3}$ in addition to the α-$Bi_2O_3$ phase (JCPDS No. 41-1449) and $Bi_2O_{2.7}$ (JCPDS No. 03-065-4028). The stability of the tetragonal phase started to deteriorate by Mo doping.[53] Upon vacuum annealing, there were no considerable changes in the phase or peak positions. Interestingly, upon performing Mo-doping, the diffraction peaks significantly broadened, along with a significant decrease in the crystallite size. As will be seen below, this is also confirmed by the SEM images showing smaller dendritic features for the Mo-doped samples. The generally observed decreased grain size of the vacuum annealed photoanodes is vital to promote more surface-active sites and thus enhance the interfacial charge-transfer rates, resulting in a superior PEC activity compared to that of an undoped or air-annealed photoanodes.

The optical nature of the fabricated photoanodes was investigated via UV-visible spectroscopy measurements. **Figure 3** shows the absorbance spectra (**Figure 3a**) for the $Bi_2O_3$, OV-$Bi_2O_3$, Mo:$Bi_2O_3$, and OV-Mo:$Bi_2O_3$ films and the Tauc plots (**Figure 3b**) used to estimate the optical bandgaps of the films. As depicted

in **Figure 3a**, all the electrodes of $Bi_2O_3$, OV-$Bi_2O_3$, Mo:$Bi_2O_3$, and OV-Mo:$Bi_2O_3$ photoanodes exhibited strong absorption in the visible region, with absorption onsets in the range between 400–490 nm. The pure vacuum untreated β-$Bi_2O_3$ film showed the poorest absorption characteristics in both optical density and absorption edge. After vacuum annealing, the absorption edge is red-shifted with a considerable increase in the optical density above the bandgap. The red-shifting of the bandgap can be partially explained by the lattice expansion noticed in the XRD results. Most importantly, oxygen vacancies, especially those at the surface, can create shallow levels at the conduction band edge reducing the effective bandgap of the material.[54]

For the Mo-doped vacuum untreated α-$Bi_2O_3$, there is a remarkable effect of the Mo-doping in both reducing the bandgap and increasing the optical density. The ionic radius of Mo is almost half that of Bi.[53] The bandgap reduction can, therefore, be an indication of interstitial doping of Mo ions rather than direct substitution of Bi sites, which would have slightly increased the bandgap. Upon annealing, the optical density increased with a large red-shift of the absorption edge that can be noticeably seen as a long absorption tail. This absorption tail can be attributed to the combined effect of shallow energy levels created by oxygen vacancies and the lattice distortion created by Mo doping. The reported values for the bandgaps of different $Bi_2O_3$ phases varied greatly in the literature, where the preparation method played an important role on determining the bandgap. Values between ~ 2-4 eV were reported for the α and β-$Bi_2O_3$ phases.[11-13,19,55] Among these methods, thermal oxidation of a previously prepared Bi film, which is close to the preparation conditions in our case, showed a considerable disagreement of reported values.[12-14] For our samples, the bandgaps of the prepared $Bi_2O_3$, OV-$Bi_2O_3$, Mo:$Bi_2O_3$, and OV-Mo:$Bi_2O_3$ electrodes were estimated by the Tauc plots in **Figure 3b** to be 3.2, 3.1, 2.8, and 2.6 eV, respectively. Remarkably, the combined effect of Mo-doping and vacuum annealing could reduce the bandgap by more than 0.5 eV, allowing solar optical absorption in the visible range.

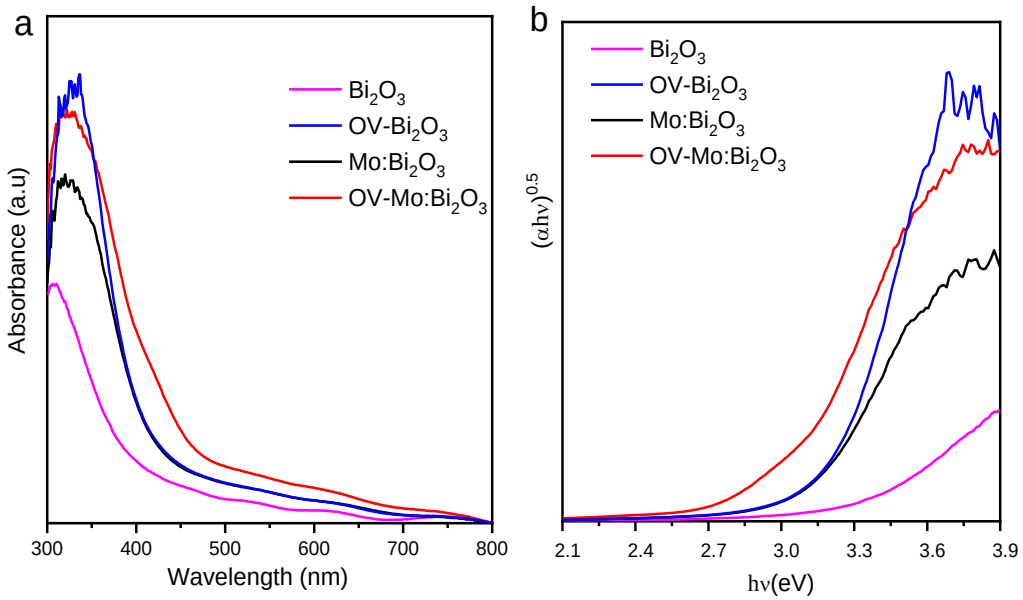


**Figure 3. Optical properties of photoanodes:** (a) Diffuse reflectance spectra of undoped $Bi_2O_3$; oxygen-deficient OV-$Bi_2O_3$, Mo:$Bi_2O_3$, and oxygen-deficient OV-Mo:$Bi_2O_3$ photoanodes; (b) Tauc plots of $(\alpha h\nu)^{1/2}$ vs. the energy of the light absorbed for the fabricated photoanodes.

**Figure 4** depicts the FE-SEM images of the nanostructured $Bi_2O_3$ electrodes with and without the optimum Mo-doping for two different thermal processes (air and vacuum). All films have randomly arranged dendrites with a micro-nano hierarchical structure. Dendritic structured photoanodes have been the main focus for many researchers because of their excellent connectivity between the crystals, making them effective photoanodes.[59-61] Especially, the inter-leaf spacing in this 3D nanostructure offers a favorable pathway for electrolyte ions; therefore, more electrochemically active sites, as well as minor branches, will decrease the internal resistance.[20] For the undoped samples (Figure 4a, b), the stems in the dendrites are in the range of 1–2 μm in length with many side nano-branches less than 200 nm long. Interestingly, Mo-doping (Figure 4c,d) resulted in reduced dimensions of the dendritic network, confirming the broader XRD peaks mentioned above. This would have resulted in a more substantial surface area and, therefore, more active surface sites for the PEC reactions, as revealed by the PEC behavior of photoanodes mentioned below. For both Mo-doped and undoped samples, vacuum treatment had resulted in virtually no morphological changes in the photoanodes. Finally, the elemental mapping of the OV-Mo: $Bi_2O_3$ dendritic structures are depicted in **Figure S1,** unambiguously confirming the existence of constituent elements, namely, Mo and Bi, in the tested photoanodes.

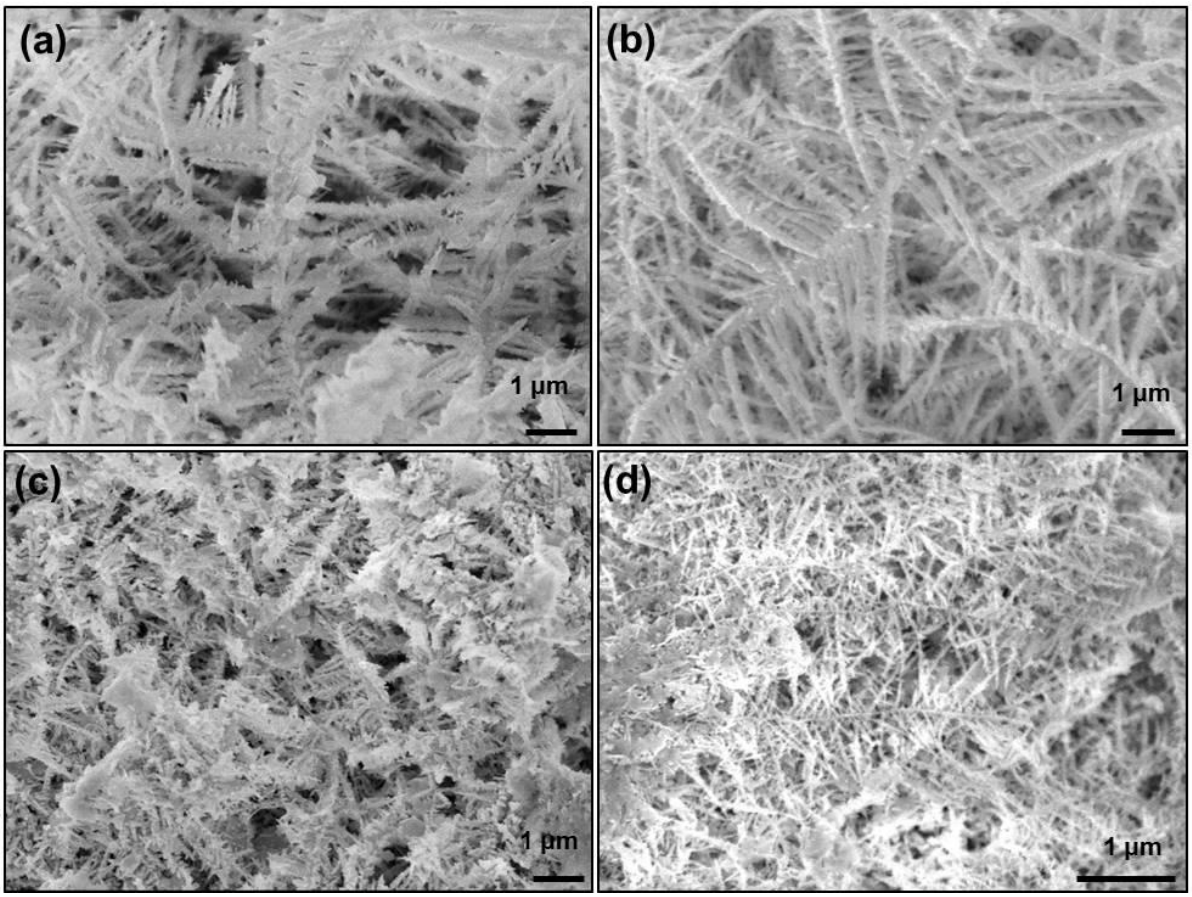


**Figure 4. Morphological characteristics of photoanodes.** FE-SEM micrographs of (a) nanostructured $Bi_2O_3$ photoanodes fabricated using electrodeposition on FTO substrates, (b) oxygen-deficient OV-$Bi_2O_3$ photoanodes fabricated after vacuum-annealing, (c) FE-SEM images of dendritic-structured Mo:$Bi_2O_3$ on FTO, and (d) FE-SEM images of OV-Mo:$Bi_2O_3$ photoanodes fabricated using electrodeposition followed by vacuum-annealing.

**Figure 5** shows the XPS spectra of Bi 4f and O1s of bare $Bi_2O_3$ and OV-$Bi_2O_3$. The Bi $4f_{7/2}$ and Bi $4f_{5/2}$ doublets positioned at 159.6 eV and 165.1 eV respectively indicate the $Bi^{3+}$ oxidation state and successful formation of $Bi_2O_3$.[56,57] The two samples showed no appreciable changes in the Bi 4f region (**Figure 5a**). The O1s spectra showed, in addition to the ~ 529 eV peak corresponding to oxygen in the lattice ($O_L$), another higher energy peak ($O_V$) at ~ 531 eV (**Figure 5b**), which is attributed to oxygen vacancies on the surface.[56-58] Interestingly, the $O_V$ contribution in the OV-$Bi_2O_3$ sample is remarkably more significant compared to the bare $Bi_2O_3$ indicating the existence of chemisorbed oxygen that is caused by existing oxygen vacancies on the surface.[56,57] From the integrated areas of respective oxygen peak components, the $O_V/O_L$ ratio is estimated to be ~ 0.4 and 1 for the bare $Bi_2O_3$ and OV-$Bi_2O_3$, respectively. As mentioned above, this increase of surface oxygen vacancy sites can also contribute to enhancing the photocatalytic activity, which was observed in the PEC experiments below.

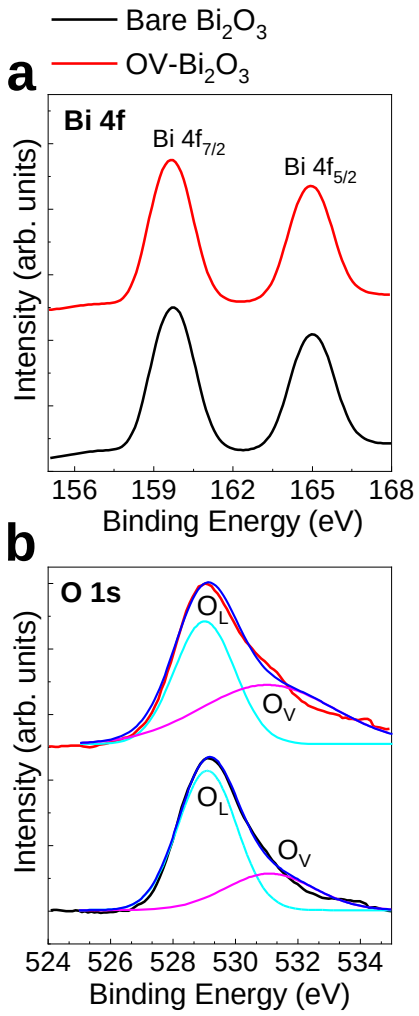


**Figure 5. Surface characterization of electrodes.** High-resolution XPS results on Bi 4f (a) and O 1s orbital (b) for bare $Bi_2O_3$ and OV-$B_{i2}O_3$ electrodes

***PEC behavior of photoanodes***

**Figure 6a** depicts the linear sweep volumetric (LSV) PEC behavior of the four samples. First, distinctive LSV plot data indicate that the photoanodes have no photo-activity under dark conditions. The sole $Bi_2O_3$ without any dopant or surface activation exhibited almost no photocurrent over the whole 0-1.23V region (**Figure 6a**), indicating that $Bi_2O_3$ is not photoactive. Vacuum annealing alone resulted in a fair improvement of the photocurrent, while Mo-doping alone resulted in a more significant contribution. The combined effect of both Mo-addition and vacuum-annealing resulted in superior photocurrents as compared to those in OV-$Bi_2O_3$, Mo:$Bi_2O_3$, and undoped $Bi_2O_3$. For comparison, at the potential of 1.23 $V_{RHE}$, the photoanodic current densities of the sole-$Bi_2O_3$, OV-$Bi_2O_3$, Mo:$Bi_2O_3$, and OV-Mo:$Bi_2O_3$ photoanode films were 0.04, 0.16, 0.49, and 1.06

mA·cm$^{-2}$, respectively. Therefore, the synergetic effect of vacuum annealing and Mo-doping could successfully offer an efficient photoanode treatment strategy boosting the generated photocurrent by > 25-fold.

The role of vacuum annealing and Mo-incorporation was also investigated under chopped 1-sun illumination conditions. **Figure 6b** represents the comparative LSV plots under chopped illumination with a fixed time interval for the OV-Mo:$Bi_2O_3$ photoanode film in comparison with bare $Bi_2O_3$. From the figure, the photocurrent performance of the OV-Mo:$Bi_2O_3$ photoanode increases at all applied bias. However, for the OV-Mo:$Bi_2O_3$ photoanode film, the observed photocurrent of the chopped light of LSV is almost linear, which is reached instantly upon turning on the light. This typical behavior is similar to earlier reports on CoPi-loaded electrodes evaluated in the presence of an electrolyte comprising a fast redox shuttle.[3] On the other hand, shifting of the onset of photocurrent to the lower potential region through vacuum annealing and Mo-doping, as shown in **Figure 6b**, demonstrates the photocatalytic behavior of Mo in an aqueous medium.[6,8] The observed PEC enhancement for the OV-Mo:$Bi_2O_3$ photoanodes can be credited mainly to the increased PEC active sites generated by the higher surface area of Mo-doped samples and by the surface OVs created y vacuum annealing. Moreover, the more definite current transients between 0.5 and 1.7 V for the OV-Mo:$Bi_2O_3$ photoanodes suggest that the photoinduced carriers live longer after vacuum annealing and Mo incorporation.

This substantial enhancement in the photocurrent density is supplemented by a considerable cathodic shift in the photocurrent-onset potential. Furthermore, a considerable photocurrent density was attained in the lower bias region (0.6 $V_{RHE}$) in all photoanodes, as depicted in **Figure S2**, whis is very interesting for tandem photoanode-photocathode configurations.

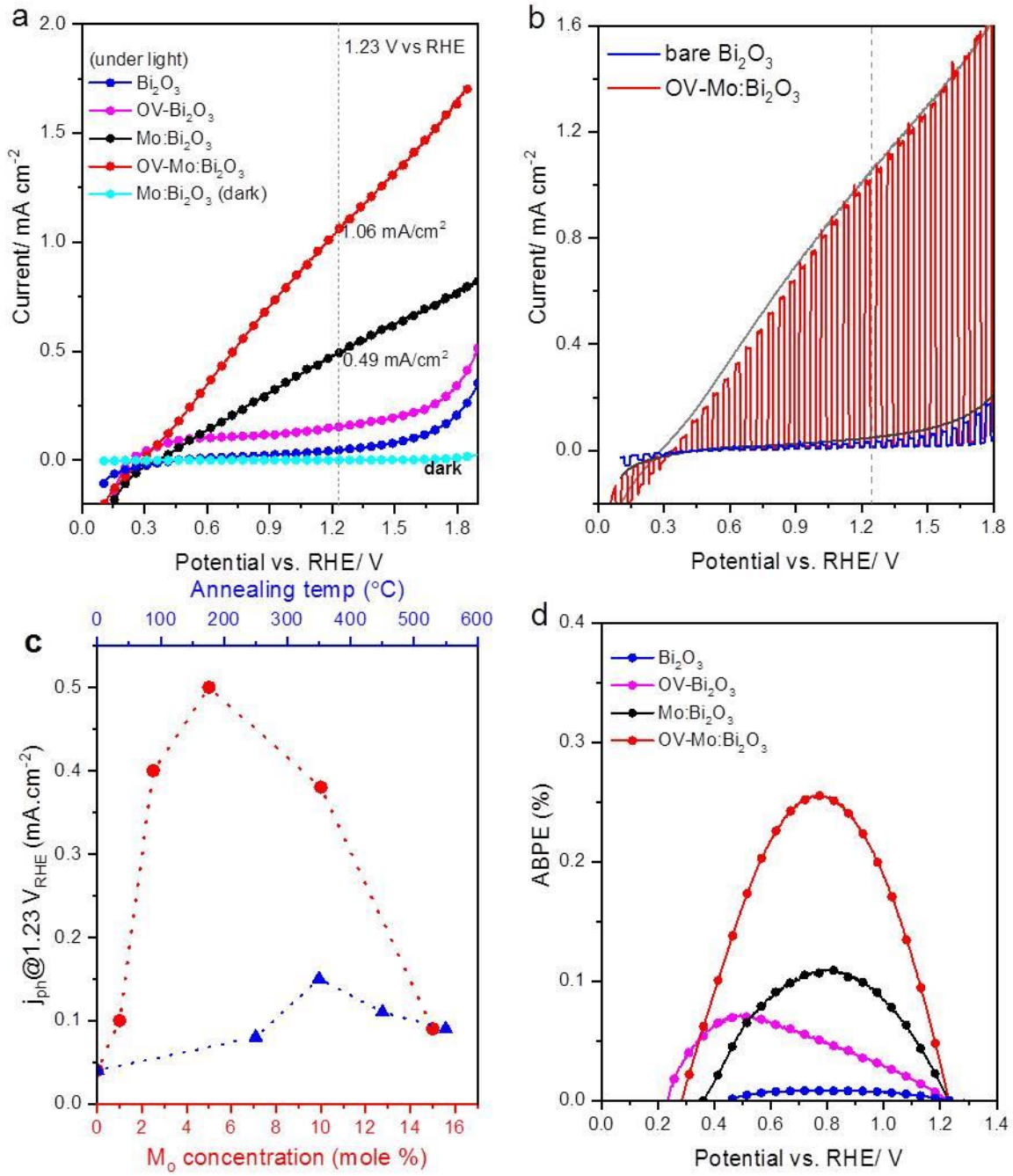


**Figure 6. PEC nature of photoanodes.** (a) Photocurrent-potential features for undoped $Bi_2O_3$, oxygen-deficient OV-$Bi_2O_3$, Mo-doped $Bi_2O_3$, i.e., Mo:$Bi_2O_3$, and oxygen-deficient OV-Mo: $Bi_2O_3$ photoanodes in the PBS (0.1 M, pH 7.5) measured under constant (b) J-V curve of the optimized OV-Mo:$Bi_2O_3$ photoanodes in comparison with bare $Bi_2O_3$ under chopped illumination condition. (c) Photocurrent-potential characteristics at 1.23 V versus RHE for different Mo-doping concentrations (red symbols) and different annealing conditions (blue symbols) in the PBS solution at pH 7.5, and (d) equivalent applied-bias photon-to-current efficiency of the fabricated photoanodes.

Finally, **Figure 6c** presents the generated photocurrent at 1.23 $V_{RHE}$ under different Mo doping and vacuum annealing temperatures, signifying that the best performance was obtained for 5.0 mole% Mo and vacuum annealing at 350 °C, which are the optimum conditions used for the electrodes in **Figure 6a**. To evaluate the solar conversion efficiency of the photoanodes, the ABPE was assessed versus the applied bias and are depicted in **Figure 6d**. The estimated photoconversion efficiencies were only 0.01% and 0.05% at 0.8 $V_{RHE}$ for the undoped $Bi_2O_3$ and OV-$Bi_2O_3$ electrodes, respectively. However, with Mo-doping, the higher conversion efficiency of 0.1% at 0.8 $V_{RHE}$ was achieved for Mo:$Bi_2O_3$ film, which was further enhanced to 0.26% at 0.8 $V_{RHE}$ after vacuum annealing. These results also confirm that the combination of optimal Mo-doping and vacuum-annealing conditions synergistically improved the PEC performance.

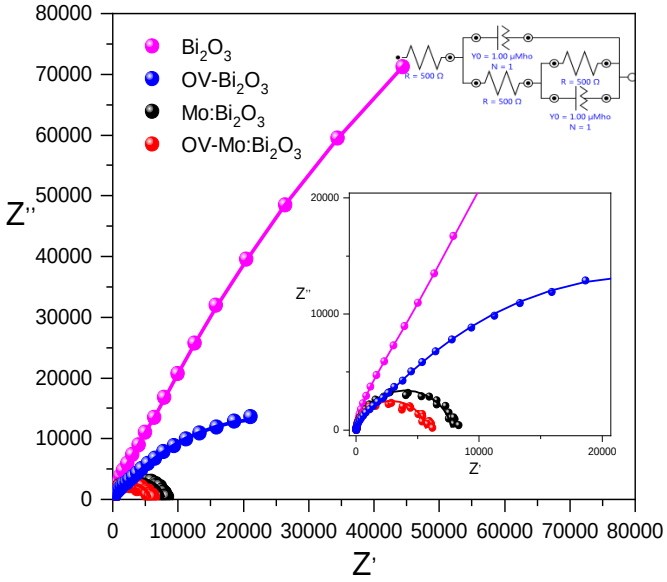


**Figure 7. Electrochemical impedance investigation.** Nyquist plots electrochemically deposited undoped $Bi_2O_3$, oxygen-deficient OV-$Bi_2O_3$, Mo-doped Mo:$Bi_2O_3$, and oxygen-deficient OV-Mo:$Bi_2O_3$ photoanodes. The impedance analysis was completed at 1.0 $V_{RHE}$ in the frequency varying from 100, 000 to 0.05 Hz, and the figure inset shows the equivalent circuit and its enlarged view.

Furthermore, EIS analysis was performed to examine the charge-transfer kinetics at the photoelectrode/electrolyte interface. The Nyquist plots of the electrodeposited photoanodes tested under constant-light conditions at 1 $V_{RHE}$ and its corresponding equivalent circuits are depicted in **Figure 7**. Mostly, the diameter of the semicircle in the higher frequency region is attributed to the charge-transfer resistance ($R_{ct}$). As seen from **Figure 7**, the radius of the arc of the Nyquist plots of the OV-Mo:$Bi_2O_3$ films is comparatively lesser than those of other fabricated photoanodes, signifying rapid interfacial charge-transfer and, also, effective separation of the

induced charge carriers. This can be attributed to the more significant number of PEC active sites generated by both the increased vacuum-generated surface VOs and the higher surface area of the Mo-doped film. Interestingly, Mo-doping enhanced both the charge-carrier density and electrical conductivity, thus lowering the resistance (**Table 1**).

**Table 1.** Impedance parameter values derived from the fitting to the equivalent circuit for the impedance spectra were examined under constant illumination condition at 1.0 V vs. RHE. Rs = solution resistance, Rct = charge-transfer resistance.

| Samples | $R_s$ (ohm) | CPE-P; n | CPE-T; Q [Ω-1s-n] | $R_{ct}$ [kΩ] |
|---|---|---|---|---|
| **$Bi_2O_3$** | 47.0 | 0.94 | $1.74*10^{-5}$ | 393 |
| **OV-$Bi_2O_3$** | 25.1 | 0.93 | $5.2*10^{-5}$ | 43.8 |
| **Mo:$Bi_2O_3$** | 41.3 | 0.92 | $2.4*10^{-10}$ | 4.76 |
| **OV-Mo:$Bi_2O_3$** | 27.9 | 0.92 | $4.7*10^{-10}$ | 3.71 |

To further gain insights into the influence of the creation of oxygen vacancies/Mo-doping on the electrical features of $Bi_2O_3$, Mott–Schottky (M-S) analysis was performed to assess the charge carrier density of the fabricated electrodes. Capacitance measurements were carried out to acquire M-S plots (**Figure 8**) at each potential with 10 kHz frequency. A detailed M-S plot of the fabricated photoanodes is discussed in supporting information. The result of the calculation is in **Table 2**. They all have positive slopes, which specify that $Bi_2O_3$ based electrode is an n-type semiconductor with electrons as the major charge carriers. In contrast to earlier works where the use of reductive atmospheres led to increased donor density,[56] this parameter did not considerably change in all tested conditions (**Table 2**), revealing that the higher density of oxygen vacancies assessed by XPS is not translated into the $Bi_2O_3$ bulk (**Figure 8a**). A similar phenomenon is observed for Mo:$Bi_2O_3$ electrodes (**Figure 8b**) and in our earlier reports on Zr-doped $TiO_2$ nanotubes.[47] The obtained donor density is almost similar before and after vacuum annealing, which can be a good indication that created oxygen vacancies are located mostly on the surface, allowing them to directly contribute to the PEC process. Further, compared with Mo:$Bi_2O_3$ sample, the OV-Mo:$Bi_2O_3$ sample exhibits a shift in the cathodic direction of 170 mV of effective $E_{FB}$, as displayed by the M-S plots of bare $Bi_2O_3$ and OV-$Bi_2O_3$ (**Table 2**). More importantly, the $E_{FB}$ is cathodically shifted upon vacuum thermal treatment, which is consistent with the cathodic shift of the photocurrent onset potential for the optimal combination in **Figure 6a**. A cathodic shift in $V_{FB}$ is advantageous for electrons to pass through the circuit to the counter electrode, thus resulting in decreasing the onset potential for anodic photocurrent. Clearly, the charge carrier density has been dramatically increased after Mo doping (**Figure 8c**, **Table 2**). It further verified

that Mo is a shallow donor in doped $Bi_2O_3$ films. All the obtained results clearly revealed the introduction of oxygen vacancies and Mo-doping influence the PEC performance deeply.

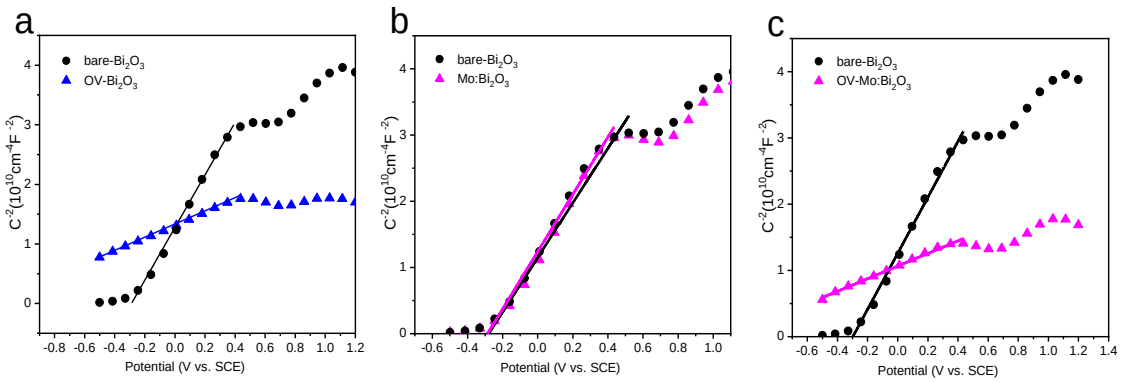


**Figure 8**. Mott-Schottky (M-S) plots of the capacitance of bare-$Bi_2O_3$ (a) electrodes thermally treated in air and vacuum, and comparison with Mo doped bare-$Bi_2O_3$ (b), comparative M-S plots of bare-$Bi_2O_3$ and Mo:$Bi_2O_3$ thermally annealed in vacuum.

**Table 2.** Parameters obtained from the Mott-Schottky performances obtained from **Figure 8**

| Samples | $E_{FB}$ (V vs. SCE) | Donor density ($cm^{-3}$) |
|---|---|---|
| **bare-$Bi_2O_3$** | -0.28 V | **$8.82 \times 10^{19}$** |
| **OV-$Bi_2O_3$** | -0.31 V | **$9.25 \times 10^{19}$** |
| **Mo:$Bi_2O_3$** | -0.65 V | **$3.89 \times 10^{20}$** |
| **OV-Mo:$Bi_2O_3$** | -0.82 V | **$3.59 \times 10^{20}$** |

The long-term stabilities of undoped OV-$Bi_2O_3$, Mo:$Bi_2O_3$, and OV-Mo:$Bi_2O_3$ photoanodes were comparatively evaluated in the PBS solution for more than 5 h at 1.23 $V_{RHE}$ under constant-light conditions (see **Figure 9)**. Notably, the observed photocurrent values were in agreement with the results acquired from the corresponding LSV-plots. The photocurrent density of undoped OV-$Bi_2O_3$ declined from 0.20 to 0.05 mA/$cm^2$ under constant-light conditions for 5 h (i.e., 75% loss), because the undoped OV-$Bi_2O_3$ suffered not only from the incessant illumination-induced photocorrosion but also from the chemical corrosion due to $H_2O_2$, owing to oxygen reduction on the $Bi_2O_3$ surface.[63] The observed results are consistent with those in earlier research works.[64,65] The vacuum-annealed OV-Mo:$Bi_2O_3$ thin films, which signify the combined effect of both Mo-doping and vacuum-annealing, could sustain a significant photocurrent density after 5 h of approximately 0.95 mA·$cm^{-2}$, corresponding to ~ 92%

of its original value. Furthermore, the photocurrent loss over time takes place mainly in the first 10-20 minutes with no visible sign of long-term decay after 5 h, suggesting substantial long-lasting durability of the photoanodes. Furthermore, under an on-off switching, the current density was abruptly retained with even slight improvement. The investigation, as mentioned above, evidenced that the synergetic effect of both the optimal Mo-doping and vacuum-annealing conditions in OV-Mo:$Bi_2O_3$ photoanodes enhanced both the PEC performance and the stability of the photoanodes.

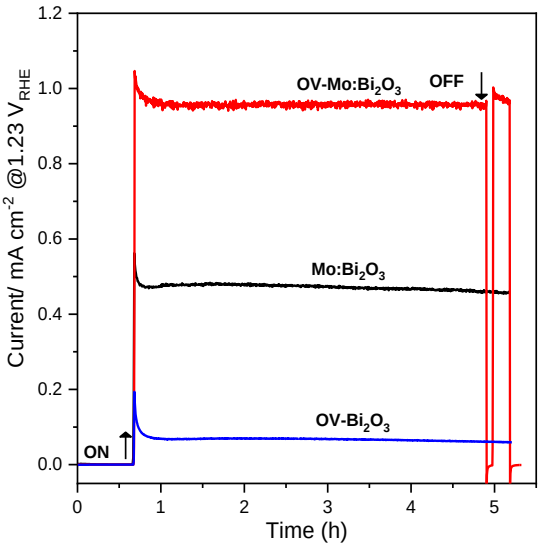


**Figure 9. Durability investigation of photoanodes.** J–t curves for long-standing photostabilities of OV-Mo: $Bi_2O_3$ thin-film electrodes (red), Mo:$Bi_2O_3$ electrodes (black), and undoped OV-$Bi_2O_3$ (blue) measured in the PBS solution (0.1 M, pH 7.5) at 1.23 $V_{RHE}$ under illumination conditions.

## 4. Conclusions

We fabricated nanostructured oxygen-deficient OV-Mo:$Bi_2O_3$ photoanodes via simple electrochemical deposition followed by post-annealing under vacuum. Notably, we revealed that the synergetic effect of Mo-doping and vacuum-annealing improved the surface activity of the nanostructured $Bi_2O_3$ films, leading to enhanced PEC water-oxidation performance. Both Mo-doping and vacuum-annealing resulted in a more effective $Bi_2O_3$ surface, which resulted first in the establishment of surface defects (OVs), thereby enhancing the carrier transport. Also, Mo-doping is revealed to increase the surface area of the prepared films, further increasing the active sites that are in contact with the electrolyte. This combined effect of both Mo-doping and vacuum-annealing in optimized OV-Mo:$Bi_2O_3$ photoanodes demonstrated a nearly 25-fold improvement, as compared with undoped $Bi_2O_3$ increasing the photocurrent density from 0.05 mA.cm$^{-2}$ to approximately 1.06 mA·cm$^{-2}$ at 1.23 $V_{RHE}$ .

## Credit authorship contribution statement

Maged N. Shaddad: Data curation, Formal analysis, Investigation, Writing - original draft. Prabhakarn Arunachalam: Conceptualization, Data curation, Formal analysis, Investigation, Supervision. Writing - review & editing. Mohmoud Hezam: Investigation, Conceptualization. Norah M. AL-Saeedan: Formal analysis; Sixto Gimenez: Supervision, Juan Bisquert: Supervision Abdullah M. Al-Mayouf: Supervision, Funding acquisition, Project administration.

## Declaration of Competing Interest

The authors declare that they have no known competing financial interests or personal relationships that could have appeared to influence the work reported in this paper.

## Acknowledgments

This project was funded by the National Plan for Science, Technology, and Innovation (MAARIFAH), King Abdulaziz City for Science and Technology, Kingdom of Saudi Arabia, Award Number (14-NAN2323-02).

## References

[1] M. Grätzel, Photoelectrochemical cells, Nature 414 (2001) 338–344.

[2] A. Fujishima and K. Honda, Electrochemical photolysis of water at a semiconductor electrode, Nature 238 (1972) 37–38.

[3] B. Klahr, S. Gimenez, F. Fabregat-Santiago, J. Bisquert, T. W. Hamann, Photoelectrochemical and impedance spectroscopic investigation of water oxidation with “Co–Pi”-coated hematite electrodes, J. Am. Chem. Soc. 134 (2012) 16693-16700.

[4] R. Saito, Y. Miseki, and K. Sayama, Highly efficient photoelectrochemical water splitting using a thin film photoanode of BiVO 4/SnO 2/WO 3 multi-composite in a carbonate electrolyte, Chem. Commun. 48 (2012) 3833–3835.

[5] F.F. Abdi, L. Han, A.H. Smets, M. Zeman, B. Dam, and R. van de Krol, Efficient solar water splitting by enhanced charge separation in a bismuth vanadate-silicon tandem photoelectrode, Nat. Commun. 4 (2013) 2195.

[6] S.C. Riha, B. M. Klahr, E. C. Tyo, S. Seifert, S. Vajda, M. J. Pellin, T.W. Hamann, A. B. Martinson, Atomic layer deposition of a submonolayer catalyst for the enhanced photoelectrochemical performance of water oxidation with hematite, Acs Nano 7 (2013) 2396-2405.

[7] M. R. Hoffmann, S. T. Martin, W. Y. Choi, and D. W. Bahnemann, Environmental Applications of Semiconductor Photocatalysis, Chem. Rev. 95 (1995) 69.

[8] P. Dai, W. Li, J. Xie, Y. He, J. Thorne, G. McMahon, J. Zhan, D. Wang, Forming buried junctions to enhance the photovoltage generated by cuprous oxide in aqueous solutions, Angew. Chem. Int. Ed. 53 (2014) 13493-13497.

[9] G. Guenther, R. Theissmann, O. Guillon, Size-dependent phase transformations in bismuth oxide nanoparticles. II. Melting and stability diagram, J. Phys. Chem. C 118 (2014) 27020-27027.
[10] M. Weber, M. Schlesinger, M. Mehring, Evaluation of synthetic methods for bismuth (III) oxide polymorphs: Formation of binary versus ternary oxides, Crystal Growth & Design 16 (2016) 5678-5688.
[11] S. Condurache-Bota, N. Tigau, A. P. Rambu, G. G. Rusu, G. I. Rusu, Optical and electrical properties of thermally oxidized bismuth thin films, Appl. Surf. Sci. 257 (2011) 10545-10550.
[12] T. P. Gujar, V. R. Shinde, C. D. Lokhande, Spray pyrolysed bismuth oxide thin films and their characterization, Mater. Res. Bull. 41 (2006) 1558-1564.
[13] L. Leontie, M. Caraman, M. Alexe, C. Harnagea, Structural and optical characteristics of bismuth oxide thin films, Surf. Sci. 507 (2002) 480-485.
[14] Y. Wang, Z. Cui, Y. Xue, R. Zhang, A. Yan, Size-Dependent Thermodynamic Properties of Two Types of Phase Transitions of Nano-Bi2O3 and Their Differences, J. Phys. Chem. C 123 (2019) 19135-19141.
[15] J. Zhang, W. Dang, X. Yan, M. Li, H. Gao, and Z. Ao, Doping indium in β-Bi 2 O 3 to tune the electronic structure and improve the photocatalytic activities: first-principles calculations and experimental investigation, Phys. Chem. Chem. Phys. 16 (2014) 23476–23482.
[16] J. Hou, C. Yang, Z. Wang, W. Zhou, S. Jiao, and H. Zhu, In situ synthesis of α–β phase heterojunction on Bi2O3 nanowires with exceptional visible-light photocatalytic performance, Appl. Catal. B Environ. 142 (2013) 504–511.
[17] X. Xiao, R. Hu, C. Liu, C. Xing, C. Qian, X. Zuo, J. Nan, and L. Wang, Facile large-scale synthesis of β-Bi2O3 nanospheres as a highly efficient photocatalyst for the degradation of acetaminophen under visible light irradiation, Appl. Catal. B Environ. 140 (2013) 433–443.
[18] J. C. Medina, M. Bizarro, C. L. Gomez, O. Depablos-Rivera, R. Mirabal-Rojas, B.M. Monroy, A. Fonseca-Garcia, J. Perez-Alvarez, and S. E. Rodil, Sputtered bismuth oxide thin films as a potential photocatalytic material, Catal. Today 266 (2016) 144–152.
[19] L. Kumari, J.-H. Lin, and Y.-R. Ma, One-dimensional Bi2O3 nanohooks: synthesis, characterization and optical properties, J. Phys. Condens. Matter 19 (2007) 406204.
[20] V.P. Zhukov, V.M. Zhukovskii, V.M. Zainullina, and N.I. Medvedeva, Electronic structure and chemical bonding in bismuth sesquioxide polymorphs, Struct. Chem. 40 (1999) 831–837.
[21] D. D'Angelo, S. Filice, A. Scarangella, D. Iannazzo, G. Compagnini, and S. Scalese, Bi2O3/Nexar® polymer nanocomposite membranes for azo dyes removal by UV–vis or visible light irradiation, Catal. Today 321-322 (2019) 158-163.
[22] K.S. Al-Namshah and R.M. Mohamed, Nd-doped Bi2O3 nanocomposites: simple synthesis and improved photocatalytic activity for hydrogen production under visible light, Appl. Nanosci. 8 (2018), 1233–1239.
[23] Y. Bao, T.-T. Lim, Z. Zhong, R. Wang, and X. Hu, Acetic acid-assisted fabrication of hierarchical flower-like Bi2O3 for photocatalytic degradation of sulfamethoxazole and rhodamine B under solar irradiation, J. Colloid Interface Sci. 505 (2017) 488–499.
[24] E. W. Bohannan, C. C. Jaynes, M. G. Shumsky, J.K. Barton, J.A. Switzer, Low-temperature electrodeposition of the high-temperature cubic polymorph of bismuth (III) oxide, Solid State Ionics 131 (2000) 97–107.
[25] X. Li, Y. Sun, T. Xiong, G. Jiang, Y. Zhang, Z. Wu, F. Dong, Activation of amorphous bismuth oxide via plasmonic Bi metal for efficient visible-light photocatalysis, J. Catal. 352 (2000) 102–112.
[26] Y. Qiu, M. Yang, H. Fan, Y. Zuo, Y. Shao, Y. Xu, X. Yang S. Yang, Nanowires of α-and β-Bi 2 O 3: phase-selective synthesis and application in photocatalysis, CrystEngComm 13(2011) 1843-1850.

[27] S. P. Adhikari, H. Dean, Z. D. Hood, R. Peng, K. L. More, Ilia lvanov, Z. Wu, A. Lachgar, Visible-light-driven Bi2O3/WO3 composites with enhanced photocatalytic activity, RSC Adv. 5 (2015) 91094–91102.
[28] C. Wang, C. Shao, L. Wang, L. Zhang, X. Li, Y. Liu, Electrospinning preparation, characterization and photocatalytic properties of Bi2O3 nanofibers, J Colloid Interface Sci. 333 (2009) 242–248.
[29] L. Leontie, M. Caraman, M. Alexe, and C. Harnagea, Structural and optical characteristics of bismuth oxide thin films, Surf. Sci. 2002, 507, 480–485.
[30] S. Koçyigit, Boron and praseodymium doped bismuth oxide nanocomposites: Preparation and sintering effects, J. Alloys Compd. 2018, 740, 941–948.
[31] P. Hajra, S. Shyamal, H. Mandal, et al. Photocatalytic activity of Bi2O3 nanocrystalline semiconductor developed via chemical-bath synthesis, Electrochim. Acta 2014, 123, 494–500.
[32] Y. Zhang, J. Lu, M. R. Hoffmann, Q. Wang, Y. Cong, Q. Wang, H. Jin, Synthesis of gC 3 N 4/Bi 2 O 3/TiO 2 composite nanotubes: enhanced activity under visible light irradiation and improved photoelectrochemical activity, RSC Adv. 2015, 5(60), 48983-48991.
[33] Y. Liu, Q. Zhao, X. Li, Y. Shi, T. Li, Vacuum-assisted impregnation derived α-Bi2O3/TiO2 nanotube arrays with enhanced photoelectrochemical activity, Materials Letters 158 (2015) 104-107.
[34] X. Zhao, H. Liu, J. Qu, Photoelectrocatalytic degradation of organic contaminants at Bi2O3/TiO2 nanotube array electrode, Appl. Surf. Sci. 257 (2011) 4621-4624.
[35] S.K. Pilli, T.E. Furtak, L.D. Brown, T.G. Deutsch, J.A. Turner, A.M. Herring, Cobalt-phosphate (Co-Pi) catalyst modified Mo-doped BiVO 4 photoelectrodes for solar water oxidation, Energy Environ. Sci. 4 (2011) 5028.
[36] F. Qin, G. Li, R. Wang, J. Wu, H. Sun, R. Chen, Template-Free Fabrication of Bi2O3 and (BiO) 2CO3 Nanotubes and Their Application in Water Treatment, Chem. Eur J. 18 (2012) 16491–16497.
[37] F. F. Abdi, N. Firet, and R. van de Krol, Efficient BiVO4 thin film photoanodes modified with Cobalt Phosphate catalyst and W-doping, Chem. Cat. Chem. 5 (2013) 490–496.
[38] J. A. Seabold, K. Zhu, and N. R. Neale, Efficient solar photoelectrolysis by nanoporous Mo:BiVO4 through controlled electron transport, Phys. Chem. Chem. Phys. 16 (2014) 1121–1131.
[39] K. P. Parmar H. Y. Kang, A. Bist, P. Dua, J. S. Jng, J. S. Lee, Photocatalytic and photoelectrochemical water oxidation over metal-doped monoclinic BiVO(4) photoanodes, ChemSusChem 5 (2012) 1926–1934.
[40] S. Kąc, T. Moskalewicz, Microstructure of doped Bi2O3 thin films deposited by PLD technique, Inżynieria Materiałowa, 34 (2013) 295-298.
[41] J. Kusiński, A. Kopia, S. Kac, A. Radziszewska, Deposition of oxide and intermetallic thin films by pulsed laser (PLD) and electron beam (PED) methods, Arch. Metall. Mater. 60 (2015) 2173–2182.
[42] H. Li, J. Shang, Z. Ai, L. Zhang, Efficient visible light nitrogen fixation with BiOBr nanosheets of oxygen vacancies on the exposed {001} facets, J. Am. Chem. Soc. 137 (2015) 6393–6399.
[43] S. Li, G. Dong, R. Hailili, L. Yang, Y. Li, F. Wang, Y. Zeng, and C. Wang, Effective photocatalytic H2O2 production under visible light irradiation at g-C3N4 modulated by carbon vacancies, Appl. Catal. B Environ. 190 (2016) 26–35.
[44] S.I. Cho, M. Logar, C.H. Lee, L. Cai, F.B. Prinz, X. Zheng, Rapid and Controllable Flame Reduction of TiO2 Nanowires for Enhanced Solar Water-Splitting, Nano letters, 14 (2013) 24-31.
[45] I.S. Cho, J. Choi, K. Zhang, S.J. Kim, M.J. Jeong, L. Cai, T. Park, X. Zheng, J.H. Park, Highly Efficient Solar Water Splitting from Transferred TiO2 Nanotube Arrays, Nano letters 15 (2015) 5709-5715.

[46] H. Song, C. Li, Z. Lou, Z. Ye, L. Zhu, Effective Formation of Oxygen Vacancies in Black TiO2 Nanostructures with Efficient Solar-Driven Water Splitting, ACS Sustain. Chem. Eng. 5 (2017) 8982-8987.

[47] D.-N. Pei, L. Gong, A.-Y. Zhang, X. Zhang, J.-J. Chen, Y. Mu, and H.-Q. Yu, Defective titanium dioxide single crystals exposed by high-energy {001} facets for efficient oxygen reduction, Nat. Commun. 6 (2015) 8696

[48] Y. Lv, W. Yao, R. Zong, and Y. Zhu, Fabrication of Wide–Range–Visible Photocatalyst Bi2WO6−x nanoplates via Surface Oxygen Vacancies, Sci. Rep. 6 (2016) 19347.

[49] Z. Zhao, Y. Zhou, F. Wang, K. Zhang, S. Yu, and K. Cao, Polyaniline-Decorated {001} Facets of Bi2O2CO3 Nanosheets: In Situ Oxygen Vacancy Formation and Enhanced Visible Light Photocatalytic Activity, ACS Appl. Mater. Interfaces 7 (2015) 730–737.

[50] M. N. Shaddad, D. Cardenas-Morcoso, M. García-Tecedor, F. Fabregat-Santiago, J. Bisquert, A. M. Al-Mayouf, and S. Gimenez, TiO2 Nanotubes for Solar Water Splitting: Vacuum Annealing and Zr Doping Enhance Water Oxidation Kinetics, ACS omega 4 (2019) 16095–16102.

[51] D. S. Aidhy, B. Liu, Y. Zhang, W. J. Weber, Chemical expansion affected oxygen vacancy stability in different oxide structures from first principles calculations, Comput. Mater. Sci. 2015, 99, 298-305.

[52] C. Cazorla, Lattice effects on the formation of oxygen vacancies in perovskite thin films, Phys. Rev. Appl. 7 (2017) 044025.

[53] R. T. Shannon, C. T. Prewitt, Revised values of effective ionic radii, ACTA CRYSTALLOGR B, 26 (1970) 1046-1048.

[54] Y. Lu, Y. Huang, Y. Zhang, J. J. Cao, H. Li, C. Bian, S. C. Lee, Oxygen vacancy engineering of Bi2O3/Bi2O2CO3 heterojunctions: Implications of the interfacial charge transfer, NO adsorption and removal, Appl. Catal. B Environ. 231 (2018) 357-367.

[55] K. Brezesinski, R. Ostermann, P. Hartmann, J. Perlich, T. Brezesinski, Exceptional Photocatalytic Activity of Ordered Mesoporous β-Bi2O3 Thin Films and Electrospun Nanofiber Mats, Chem. Mater. 22 (2010) 3079-3085.

[56] T. Qin, X. Zhang, D. Wang, T. Deng, H. Wang, X. Liu, X. Shi, Z. Li, H. Chen, X. Meng, W. Zhang, W. Zhang, Oxygen Vacancies Boost δ-Bi2O3 as a High-Performance Electrode for Rechargeable Aqueous Batteries, ACS Appl. Mater. Interfaces 11 (2018) 2103-2111.

[57] T. Xian, X. Sun, L. Di, Y. Zhou, J. Ma, H. Li, H. Yang, Carbon quantum dots (CQDs) decorated Bi2O3-x hybrid photocatalysts with promising NIR-light-driven photodegradation activity for AO7, Catalysts 9 (2019) 1031.

[58] Y. Wu, G. Lu, The roles of density-tunable surface oxygen vacancy over bouquet-like Bi 2 O 3 in enhancing photocatalytic activity, Phys. Chem. Chem. Phys. 16 (2014) 4165-4175.

[59] L.-X. Ding, F.-L. Zheng, J.-W. Wang, G.-R. Li, Z.-L. Wang, and Y.-X. Tong, Super-large dendrites composed of trigonal PbO 2 nanoplates with enhanced performances for electrochemical devices, Chem. Commun. 48 (2012) 1275.

[60] R. Zou, Z. Zhang, M. F. Yuen, J. Hu, C. Lee, and W. Zhang, Dendritic heterojunction nanowire arrays for high-performance supercapacitors, Sci. Rep. 5 (2015) 1.

[61] Z. Sun, S. Firdoz, E. Ying-Xuan, L. Li, and X. Lu, Hierarchically structured MnO 2 nanowires supported on hollow Ni dendrites for high-performance supercapacitors, Nanoscale 5 (2013) 4379.

[62] M. Wang, J. Ioccozia, L. Sun, C. Lin, Z. Lin, Correction: Inorganic-modified semiconductor TiO 2 nanotube arrays for photocatalysis, Energ. Environ. Sci. 7 (2014) 2182–2202.
[63] M. N. Shaddad, D. Cardenas-Morcoso, P. Arunachalam, M. García-Tecedor, M. A. Ghanem, J. Bisquert, A. M. Al-Mayouf, S. Gimenez, Enhancing the Optical Absorption and Interfacial Properties of BiVO4 with Ag3PO4 Nanoparticles for Efficient Water Splitting, J. Phys. Chem. C 122 (2018) 11608–11615.
[64] D. K. Zhong, S. Choi, and D. R. Gamelin, Near-Complete Suppression of Surface Recombination in Solar Photoelectrolysis by "Co-Pi" Catalyst-Modified W:BiVO4, J. Am. Chem. Soc. 133 (2011) 18370–18377.
[65] M. N. Shaddad, P. Arunachalam, A. A. Alothman, A. M. Beagan, M. N. Alshalwi, and A. M. Al-Mayouf, Synergetic catalytic behavior of AgNi-OH-Pi nanostructures on Zr: BiVO4 photoanode for improved stability and photoelectrochemical water splitting performance, J. Catal. 371 (2019) 10–19.